Flexural buckling performance of concrete-filled aluminium alloy tubular columns

Evangelia Georgantzia[a], Shafayat Bin Ali[a], Michaela Gkantou[a,1], George S. Kamaris[a], Kunal D. Kansara[a] and William Atherton[a]

[a] School of Civil Engineering and Built Environment, Liverpool John Moores University, United Kingdom

ABSTRACT

The use of aluminium alloys as a structural material has recently increased because of their advantageous properties such as high strength-to-weight ratio and corrosion resistance. However, due to their low Modulus of Elasticity, instability is a major concern for aluminium alloy structural members subjected to compression. One of the ways to improve the performance of aluminium alloy hollow sections on this count is to have concrete infill within them. Past research studies have demonstrated the potential of concrete-filled aluminium tubular (CFAT) stub columns and beams to have improved structural performance, but there is still no reported research on CFAT slender columns. This paper presents an experimental and numerical investigation on the structural response of square and rectangular CFAT members under axial compression. A series of 18 tests were carried out, including nine CFAT and nine bare aluminium tubular (BAT) columns for reference purpose. The columns had pin-ended boundary conditions allowing rotation about the minor axis. The tubes were made of 6082-T6 heat-treated aluminium alloy and filled with concrete. The experimental failure modes, ultimate strengths and load versus mid-height lateral displacement curves are reported. Finite element models were developed and validated against the test results. A parametric study was subsequently conducted to study the buckling behaviour for a range of cross-sections and concrete strengths. The test and numerical results were utilised to assess Eurocode design equations for Class A aluminium alloy columns. It was shown that the current codified equations underestimate the actual strength of BAT slender columns and a new buckling curve improving the design accuracy is proposed. In absence of design provisions for CFAT columns, the design methodology of European standards for composite steel-concrete members with the

[1] Corresponding author: Michaela Gkantou
Email: m.gkantou@ljmu.ac.uk

material properties of steel replaced by those of aluminium is adopted. Finally, on the basis of the results of this study a design buckling curve suitable for CFAT columns is proposed.

Keywords: Aluminium, Tubular, Concrete-filled, Columns, Finite Element.

1. Introduction

The use of aluminium alloys in the construction sector is rising because of their profound features including good corrosion resistance, high strength-to-weight ratio, aesthetic appearance, good ductility, ease of fabrication, and high recyclability [1]. However, due to their low Modulus of Elasticity, instability is a major concern for aluminium alloy structural members. One of the ways to improve the aluminium hollow sections' performance on this count is to have concrete infill within them.

Concrete-filled steel tubular (CFST) columns are used in modern structures due to their advantages over reinforced concrete or bare steel columns. The CFST columns have higher strength, greater fire resistance, eliminate the need of temporary formwork during concrete casting and can allow for cost-effective and high-speed construction [2-7]. Despite these benefits, concerns related to the application of conventional CFST columns in composite structures include the high self-weight and the corrosion of steel tube. These issues can be overcome by replacing steel with aluminium alloys. The use of aluminium can reduce the self-weight of composite columns [8] and extend their applicability in structures located in humid environments.

In concrete-filled tubular columns, the hollow tube provides passive confinement to the concrete core [9]. At the initial elastic stage, the confining effect is small due to difference in the Poisson's ratio of the two materials. The confining pressure becomes noticeable when the lateral strain of concrete increases [10] and develops up to when concrete compressive stress achieves 80% of its unconfined strength [11]. Previous studies show that the confinement effect provided by the hollow tube significantly enhances the strength of concrete and the ductility of CFST columns [12-15]. Based on these observations, it is expected that in concrete-filled aluminium tubular (CFAT) columns, the aluminium tube will increase the compressive capacity of the concrete core due to the confinement effect, while the concrete core will delay inward local buckling of the aluminium tube.

Experimental investigations on square, rectangular and circular CFAT stub columns were firstly reported by Zhou and Young [16, 17]. It was concluded that the cross-sectional capacity of CFAT sections was improved compared to bare aluminium tubular (BAT) ones. Numerical and analytical studies on circular CFAT stub columns were also conducted by Zhou and Young [18] and Wang et al. [19]. Feng et al. [20] studied the flexural behaviour of CFAT members, concluding that the concrete infill significantly improved the stiffness, ultimate capacity and ductility of BAT flexural members. The flexural response of concrete-filled circular tubes was examined by Chen et al. [21], who demonstrated that the large thickness of the circular tubes improved the bearing capacity, ductility and bending deformation capacity of CFAT members. The structural performance of circular CFAT beams, strengthened by carbon fibre-reinforced polymer (CFRP) was evaluated by Chen et al. [22] and Zhu et al. [23]. Additional reported experimental and numerical studies on composite aluminium structures include concrete-filled double-skin aluminium tubular stub columns [24-26] and concrete-filled aluminium stub columns with synthetic (hybrid) fibre-reinforced concrete [8,27].

Past research studies have focused on the behaviour of concrete-aluminium stub columns and beams demonstrating their potential, whereas there is no reported research on the structural response of CFAT slender columns [28]. Aiming to bridge this gap, the present study reports an experimental and numerical study on CFAT slender columns with pin-ended boundary conditions. Moreover, owing to their favourable properties, such as high strength, good corrosion resistance and weldability, 6082 aluminium alloys are gaining popularity in structural applications [29, 30]. Hence this type of aluminium alloy is used herein to examine its potential as structural material. In order to examine the flexural buckling performance, Section 2 presents a series of tests on 6082-T6 heat-treated aluminium alloy square and rectangular concrete-filled and hollow columns. In Section 3, Finite element (FE) models, accounting for geometric and material nonlinearities, are developed, validated against the test data and employed in a subsequent paramedic study. Section 4 assesses current European design provisions [31, 32], whilst revised buckling curves for BAT and CFAT columns on the basis of test and FE results are proposed. Conclusions are finally summarised in Section 5.

2. Experimental programme

2.1 Test specimens

An experimental program was conducted in order to evaluate the flexural buckling performance of CFAT columns. A total of 18 tests were carried out, including nine CFAT and

nine BAT columns for reference purposes. All specimens were made of 6082-T6 heat-treated aluminium alloy and had pin-ended boundary conditions allowing rotation about the minor axis. The specimens comprised rectangular and square tubes as shown in Figure 1 and had a nominal length (L) of 1 m. The mean measured geometric dimensions of the specimens are summarised in Table 1, where D, B, t are the cross-sectional depth, width and thickness, respectively and the D/B the cross-sectional aspect ratio. The specimen designation is defined according to the cross-sectional dimensions and the presence of concrete infill. For example, the label "50.8×50.8×1.6-C" indicates a column with nominal depth of 50.8 mm, nominal width of 50.8 mm and nominal thickness of 1.6 mm. The last letter (-C) of the column label denotes the presence of concrete infill. The member slenderness ($\bar{\lambda}$) as per EN 1999-1-1 [31], ranged from 0.69 to 1.39.

The initial geometric imperfections of the aluminium alloy tubular columns can significantly influence their buckling response and maximum ultimate capacity. The initial global (ω_g) and local (ω_l) geometric imperfections were carefully measured using a linear height gauge. The measuring points were marked at 20 mm intervals along a centreline inscribed over the full length on each of the four sides of the specimens. For each side, the maximum deviation from a stable levelled surface was recorded and the maximum value amongst the four sides was reported as the local imperfection amplitude of the specimen. The initial global imperfection amplitude of the examined buckling axis, i.e. minor axis, was recorded by measuring the deviation between a point at the mid-height from a linear reference line connecting the corresponding measuring points at both ends [33]. The measured ω_g and ω_l amplitudes are listed in Table 1 and will be employed in the numerical study in the following section.

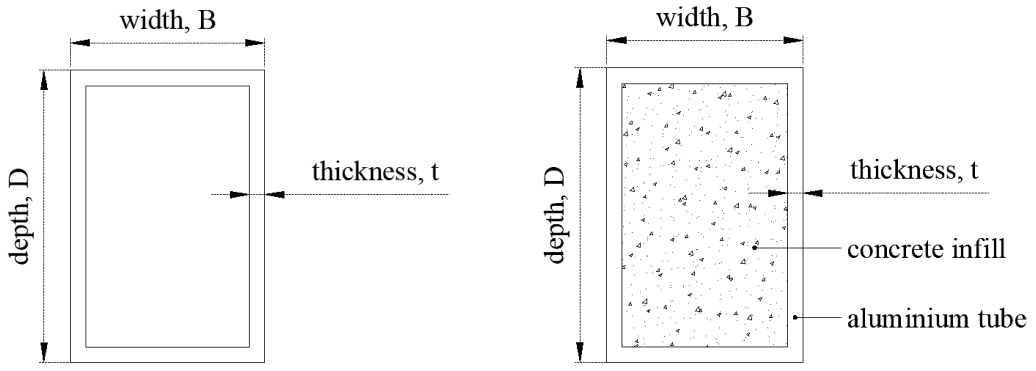

(a) BAT column (b) CFAT column

Figure 1: Geometric properties of the cross sections of the specimens.

Table 1: Mean measured dimensions and geometric imperfections of the specimens.

Specimen	D (mm)	B (mm)	t (mm)	D/B	L (mm)	ω_g (mm)	ω_l (mm)
50.8×50.8×1.6	50.7	51.0	1.61	0.99	1000.0	0.03	0.11
50.8×50.8×1.6-C	50.7	51.0	1.61	0.99	1001.0	0.09	0.28
50.8×50.8×3.3	50.6	50.6	3.13	1.00	999.0	0.04	0.170
50.8×50.8×3.3-C	50.6	50.6	3.13	1.00	1000.6	0.11	0.96
50.8×50.8×4.8	50.6	50.6	4.67	1.00	1000.0	0.01	0.19
50.8×50.8×4.8-C	50.6	50.6	4.67	1.00	999.9	0.08	0.14
76.2×76.2×3.3	76.4	76.4	3.23	1.00	1000.0	0.19	0.31
76.2×76.2×3.3-C	76.4	76.4	3.23	1.00	1000.9	0.06	0.80
76.2×76.2×4.8	76.2	76.1	4.76	1.00	1000.0	0.05	0.08
76.2×76.2×4.8-C	76.2	76.1	4.76	1.00	1001.0	0.13	0.72
76.2×76.2×6.4	76.3	76.3	6.28	1.00	1000.0	0.04	0.18
76.2×76.2×6.4-C	76.3	76.3	6.28	1.00	1000.8	0.07	0.19
76.2×38.1×3.3	76.2	38.2	3.27	1.99	1000.0	0.02	0.06
76.2×38.1×3.3-C	76.2	38.2	3.27	1.99	1001.0	0.18	0.49
76.2×50.8×3.3	76.1	50.7	3.18	1.50	1000.0	0.42	0.68
76.2×50.8×3.3-C	76.1	50.7	3.18	1.50	1000.5	0.11	0.38
101.6×50.8×3.3	101.8	51.4	3.42	1.98	1000.0	0.05	0.17
101.6×50.8×3.3-C	101.8	51.4	3.42	1.98	1000.6	0.04	0.19

2.2 Material tests

2.2.1 Aluminium 6082-T6: tensile coupon tests

Tensile coupon tests, in line with BS EN ISO 6892-1 [34], were performed to obtain the mechanical properties of the examined 6082-T6 heat-treated aluminium alloy. Two coupons were tested for each different tubular section with the nominal width and gauge length of 12 mm and 100 mm, respectively. The coupons were placed between two friction grips, as shown in Figure 2(a), and were loaded with a strain rate of 0.2 mm/min. The obtained key material properties are summarised in Table 2, including the initial Modulus of Elasticity (E_a), the 0.1% proof stress ($\sigma_{0.1}$), the 0.2% proof stress ($\sigma_{0.2}$), the ultimate tensile stress (σ_u), the strain at ultimate stress (ε_u) and the strain at fracture (ε_f). Figure 2(b) illustrates typical stress-strain curves obtained from the tensile coupon tests. The constitutive model originally proposed by Ramberg and Osgood [35] and modified by Hill [36] was used to reproduce the aluminium alloy stress-strain (σ-ε) curves according to Eqs. (1)-(2).

$$\varepsilon = \frac{\sigma}{E_a} + 0.002\left(\frac{\sigma}{\sigma_{0.2}}\right)^n \quad (1)$$

$$n = \frac{ln\,2}{ln\left(\frac{\sigma_{0.2}}{\sigma_{0.1}}\right)} \quad (2)$$

where n is the strain hardening exponent reported in Table 2.

Table 2: Measured material properties of aluminium alloy from tensile coupon tests.

Specimen	E_a (GPa)	$\sigma_{0.1}$ (MPa)	$\sigma_{0.2}$ (MPa)	σ_u (MPa)	n	ε_u (mm/mm)	ε_f (mm/mm)
50.8×50.8×1.6	65.0	284.4	289.1	315	42.3	7.5	10.5
50.8×50.8×3.3	71.7	297.5	302.2	330	44.2	7.7	9.0
50.8×50.8×4.8	67.5	302.8	305.9	325	68.1	8.8	15.5
76.2×76.2×3.3	66.2	295.2	299.1	321	52.8	7.5	10.5
76.2×76.2×4.8	64.7	303.7	306.1	316	88.1	6.3	9.7
76.2×76.2×6.4	69.3	290.4	295.3	326	41.4	8.8	15.3
76.2×38.1×3.3	68.5	270.4	276.8	315	29.6	7.8	9.3
76.2×50.8×3.3	67.5	285.9	289.5	312	55.4	7.1	9.1
101.6×50.8×3.3	60.0	176.9	183.8	225	18.1	8.2	14.9

(a) Experimental set-up

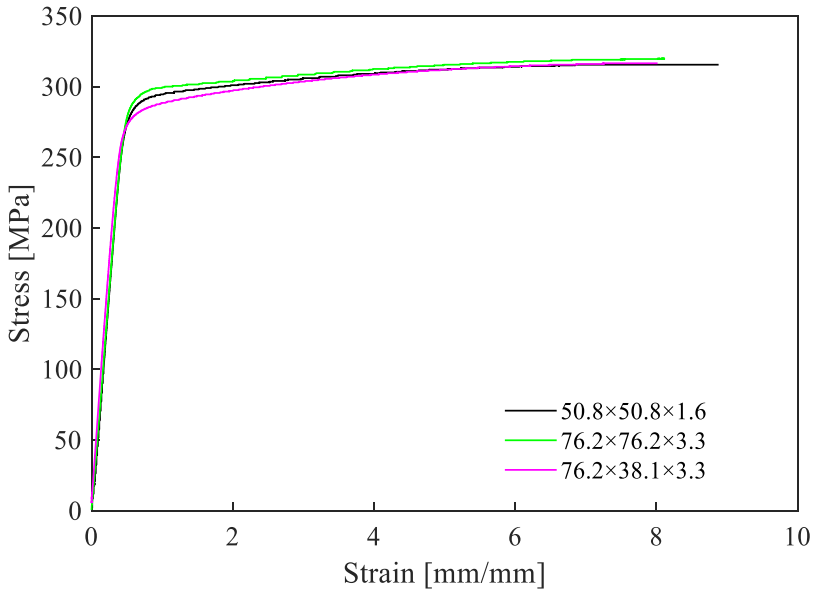

(b) Typical stress-strain curves

Figure 2: Tensile coupon tests.

2.2.2 Concrete: compressive cube tests

The concrete mix was produced using ordinary Portland cement, medium-coarse sand, coarse aggregate with a maximum size of 10 mm and freshwater with a mix ratio of 1:1.46:2.49:0.53 by weight. Four (100 × 100 × 100) mm^3 standard concrete cubes were cast from the same concrete mix used for the composite specimens and were tested under axial compression after 28 days of concrete curing. The compressive strength ($f_{ck,cube}$) of the tested cubes is listed in Table 3.

Table 3: Measured compressive strength of concrete cubes.

Specimen	$f_{ck,cube}$ (MPa)
C30-1	32.81
C30-2	32.36
C30-3	31.22
C30-4	29.87
mean	31.57

2.3 Flexural buckling tests

Before the tests, the specimens were milled flat and strengthened using CFRP wraps at both ends to prevent localised failure [17]. Furthermore, the end surfaces of the specimens with concrete infill were cast in plaster to ensure uniform distribution of the applied loading [17, 18]. An assembly of a steel plate with V-shaped grooves and a wedge plate with a single knife-edge wedge were constructed to simulate the pin-ended support conditions allowing rotation about the minor axis. Additional steel channel sections were loosely bolted through steel plates at both edges to ease the specimen's alignment into position. The compressive tests were performed using a Mayes servo-controlled hydraulic testing machine with 600 kN capacity. Each specimen was placed carefully between the two steel plates and centralised in an accurate position. Displacement control was used to drive the hydraulic actuator at a constant rate of 0.2 mm/min. Figures 3(a) and 3(b) show a photograph and an illustrative drawing of the experimental set-up, respectively. The nominal effective length of the specimen (L_{cr}), i.e. pin-to-pin distance including the knife edge set-up, was equal to 1064 mm. The instrumentation consisted of four linear variable displacement transducers (LVDTs), two at the mid-height to monitor the lateral deflection and two bilateral at the bottom edge to record the end rotation. Furthermore, four strain gauges were attached longitudinally to the four outer faces at the mid-

height to measure the in-plane and out-of-plane axial strains. The applied axial force and axial shortening were obtained by the load cell and LVDT of the testing machine, respectively. During the tests, a data acquisition system with a sampling frequency of 10 Hz was used to record all measurements. A preload of 2 kN was initially applied to achieve full contact between the pit plates and the knife-edge wedges. The actual initial load eccentricities (e_0) were determined using the LVDTs and strain gauge values measured at the beginning of tests, according to Eq. (3) [37], ensuring the initial eccentricity was less than L_{cr}/1000 [33].

$$e_0 = \frac{EI\left(\varepsilon_{max} - \varepsilon_{min}\right)}{DN} - \delta - \omega_g \tag{3}$$

where EI is the flexural rigidity of the column specimen, ε_{max} is the strain at the maximum compressive fibre, ε_{min} is the strain at the maximum tensile or minimum compressive fibre, D is the outer depth of the cross-section, N is the applied initial compressive load, δ is the lateral deflection at the mid-height and ω_g is the initial global imperfection amplitude.

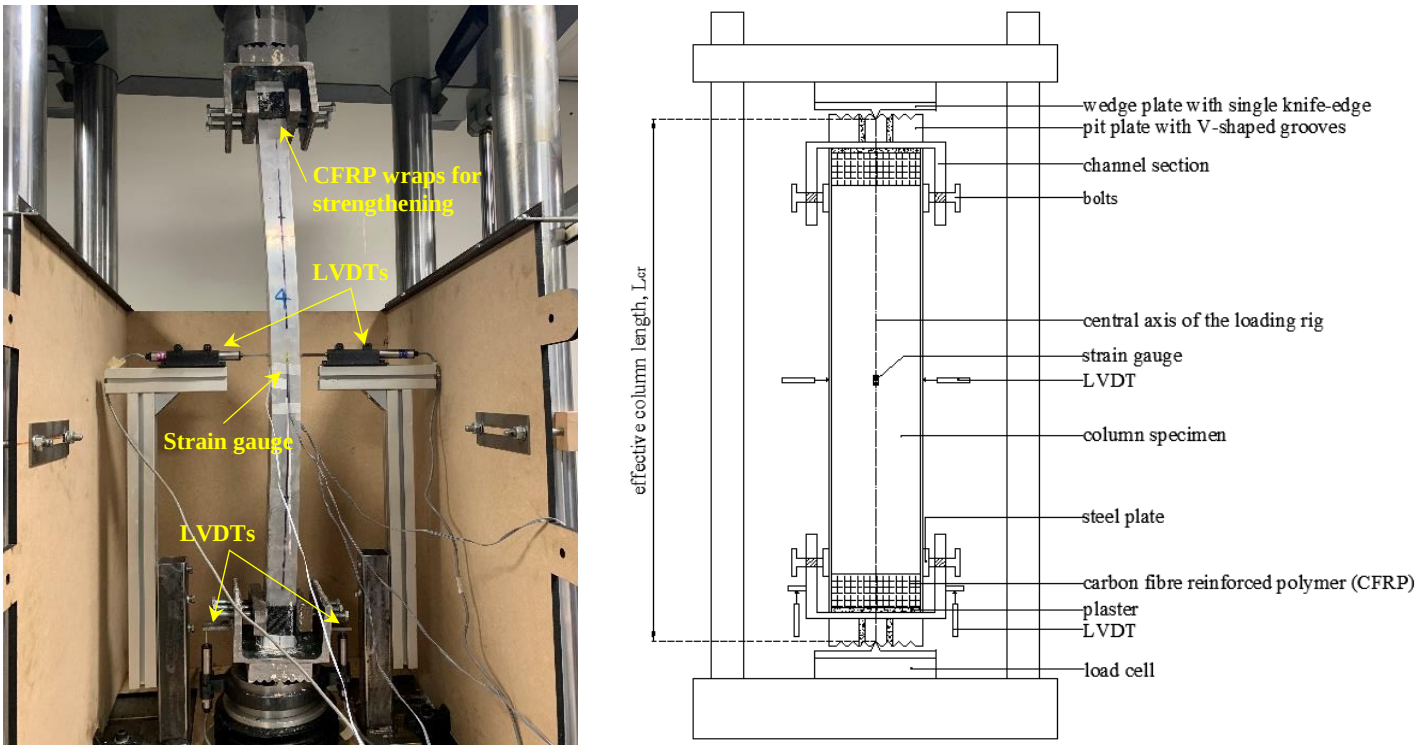

(a) photograph (b) illustrative drawing

Figure 3: Experimental set-up and instrumentation of flexural buckling tests.

As expected, the knife-edges allowed rotation about the minor axis and thus all columns failed due to flexural buckling about this axis. This was also confirmed by the out-of-plane strain

gauge values that indicated negligible out-of-plane deformations. Figure 4 shows the full-range load versus mid-height lateral deflection curves for the 18 tested specimens. The solid lines correspond to the CFAT columns while the dashed lines refer to BAT columns. It can be observed that the concrete infill improved the stiffness of the columns, as seen from the initial part of the load-deflection curves of the specimens. Furthermore, the composite columns experienced higher ultimate load compared to their bare counterparts. A typical flexural buckling mode is shown in Figure 5(a). In addition to the flexural buckling mode, upon the attainment of their ultimate load, the BAT specimens 50.8×50.8×1.6 and 76.2×76.2×3.3 with the most slender constituent plate elements also experienced local buckling at mid-height, as shown in Figure 5(b).

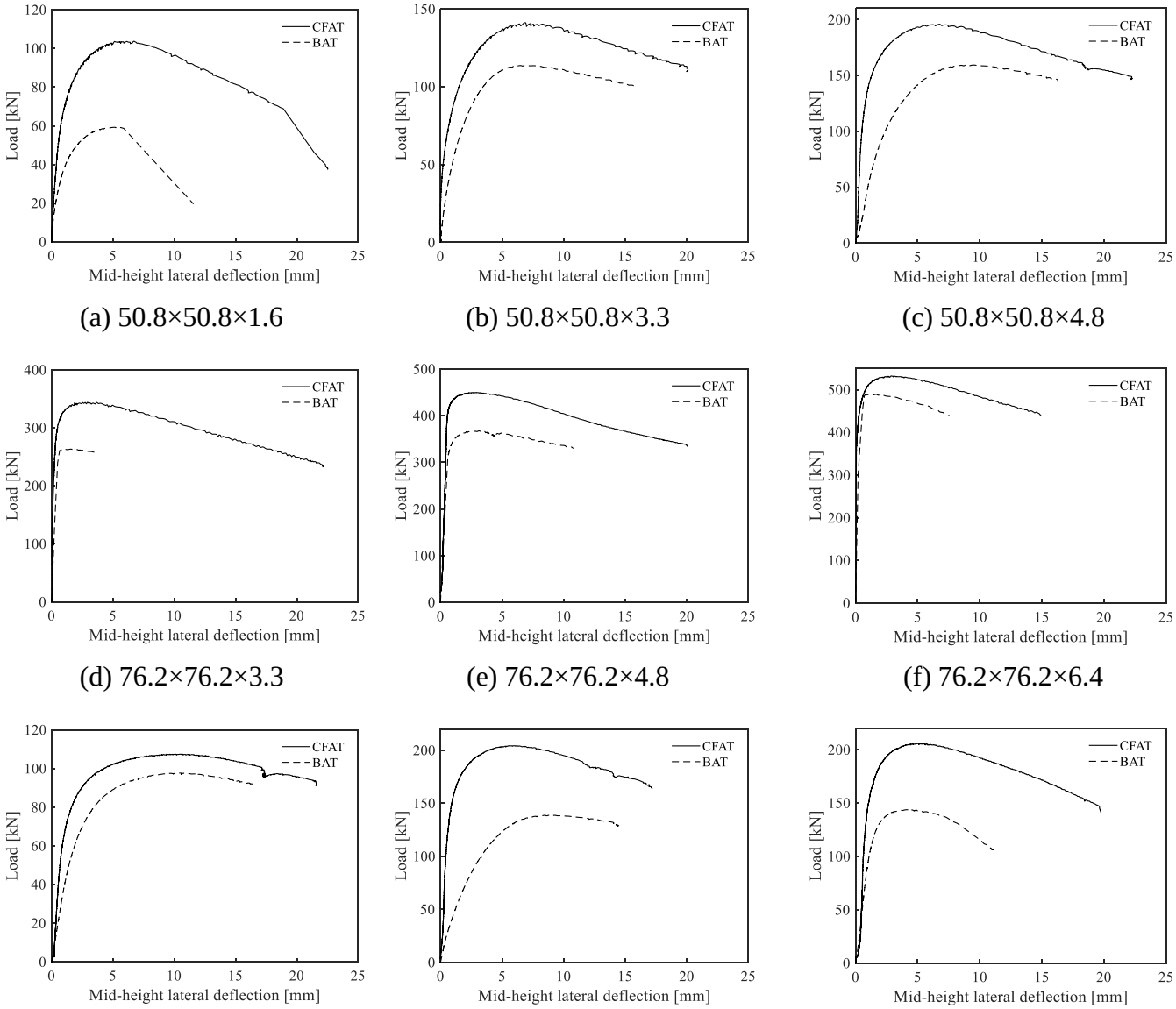

(a) 50.8×50.8×1.6 (b) 50.8×50.8×3.3 (c) 50.8×50.8×4.8

(d) 76.2×76.2×3.3 (e) 76.2×76.2×4.8 (f) 76.2×76.2×6.4

(g) 76.2×38.1×3.3 (h) 76.2×50.8×3.3 (i) 101.6×50.8×3.3

Figure 4: Load versus mid-height lateral deflection curves.

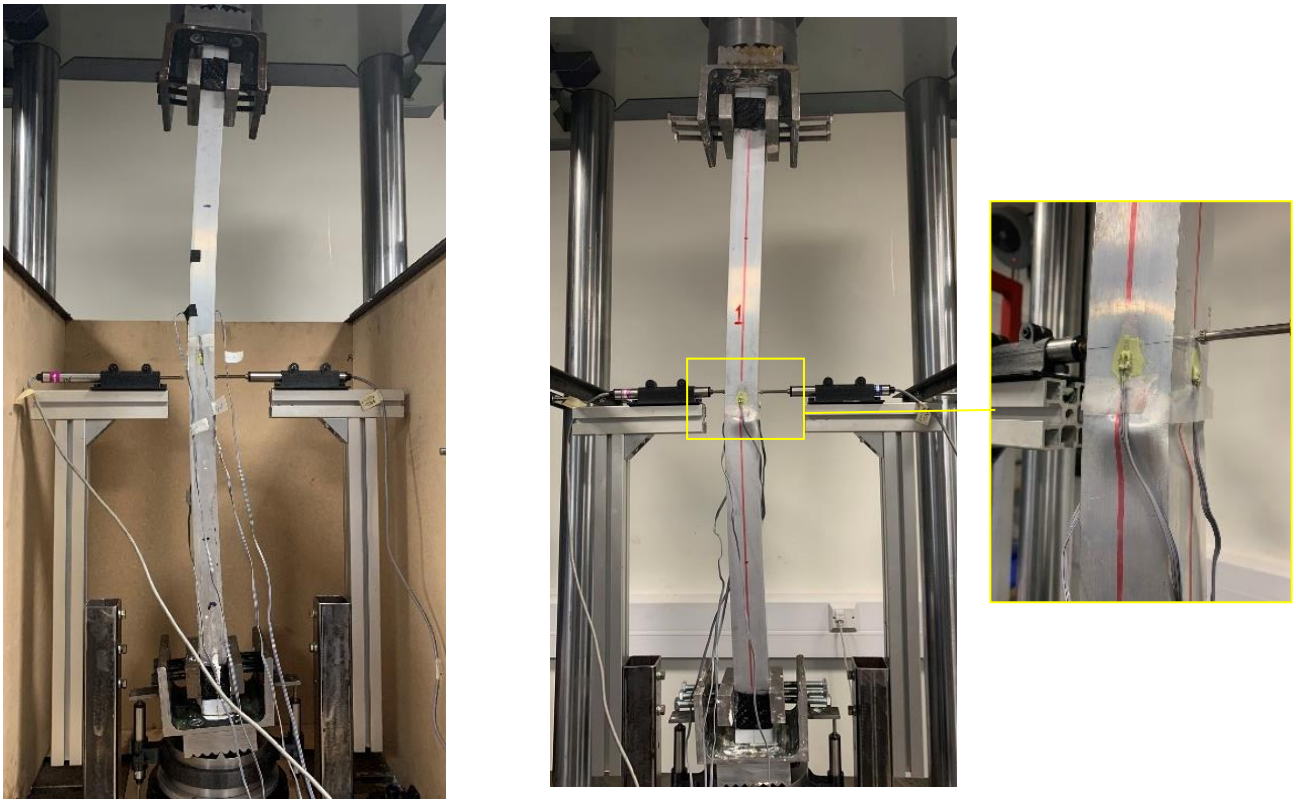

(a) 76.2×38.1×3.3-C (b) 50.8×50.8×1.6

Figure 5: Typical observed failure modes.

Table 4 presents the obtained key test results including the ultimate loads ($N_{u,Exp}$) and the lateral deflections at the mid-height corresponding to the ultimate loads (δ_u). The cross-sectional slenderness (β/ε, where $\beta = b/t$, $b = D - 2t$ and $\varepsilon = \sqrt{250/\sigma_{0.2}}$), along with the member slenderness ($\overline{\lambda}$) calculated according to [32, 33], are also included in Table 4. From the reported cross-sectional and member slenderness values, it can be seen that for constant aluminium cross-section and for constant member length, the addition of concrete infill leads to a reduction in $\overline{\lambda}$ values. This, consequently, results in increased buckling capacity of CFAT columns. To evaluate the concrete's contribution, the percentage strength increase of the ultimate load, owing to the presence of the concrete infill, is also listed in Table 4. It can be observed that the strength increase is generally higher for members with higher β/ε, i.e. thinner plate elements. The highest increase, which was equal to 72%, has been observed for specimen 50.8×50.8×1.6 and can be related to the delay in the local buckling offered by the concrete infill. The specimen 76.2×76.2×6.4 experienced the least benefit due to the concrete infill. This is related to the fact that this specimen comprises stocky aluminium plate elements

providing significant resistance to buckling and thus the increased stiffness owing to the concrete led to relatively small additional increase of the ultimate load.

Table 4: Key results from flexural buckling tests.

Specimen	$N_{u,Exp}$ (kN)	δ_u (mm)	β / ε	$\overline{\lambda}$	$N_{u,Exp}$ increase (%)
50.8×50.8×1.6	60.22	5.10	34.06	1.11	72%
50.8×50.8×1.6-C	103.71	6.69		0.98	
50.8×50.8×3.3	113.83	6.95	17.77	1.13	24%
50.8×50.8×3.3-C	141.18	6.91		1.09	
50.8×50.8×4.8	161.48	8.98	11.99	1.21	21%
50.8×50.8×4.8-C	195.77	6.76		1.18	
76.2×76.2×3.3	263.28	1.59	25.87	0.76	31%
76.2×76.2×3.3-C	344.07	2.94		0.70	
76.2×76.2×4.8	367.36	3.15	17.69	0.80	22%
76.2×76.2×4.8-C	449.68	2.89		0.76	
76.2×76.2×6.4	489.85	1.38	13.20	0.76	9%
76.2×76.2×6.4-C	532.08	2.88		0.75	
76.2×38.1×3.3	97.62	10.50	12.29	1.39	10%
76.2×38.1×3.3-C	107.47	10.10		1.38	
76.2×50.8×3.3	138.72	8.88	17.16	1.09	47%
76.2×50.8×3.3-C	204.27	5.54		1.05	
101.6×50.8×3.3	143.72	4.12	12.89	0.88	43%
101.6×50.8×3.3-C	206.15	5.25		0.87	

3. Numerical study

In parallel with the experimental investigation, a numerical study was conducted in FE software ABAQUS [38]. The developed models were validated by comparing the numerical results against the corresponding experimental data. Based on the validated models, a parametric study was performed, aiming at generating additional structural performance data over a wide range of cross-sections, member slendernesses and different concrete grades. The assumptions, techniques, accuracy of the FE models and the subsequent parametric study are described in the current section.

3.1 Modelling assumptions

FE models of CFAT and BAT columns were developed according to the measured cross-section geometries and material properties reported in Tables 1-3. Both core concrete and aluminium tube were simulated by C3D8R elements [18, 25]. A mesh sensitivity study was performed to determine the optimal element size for achieving accurate numerical results with a reasonable computational time and an average element size of 5 mm was applied. A minimum

of three elements were used to discretise the aluminium wall thickness and retain accuracy while capturing the behaviour under geometric and material nonlinearities [39].

Following ABAQUS programme's requisite protocol for simulating plasticity of the materials, the engineering stress and strain for the aluminium alloy obtained from the coupon tests were converted to true stress and logarithmic plastic strain. For aluminium, an elastic-plastic model with a von Mises yield criterion with isotropic hardening was adopted.

The concrete damaged plasticity model from ABAQUS material library was employed to simulate concrete infill's plasticity. The Modulus of Elasticity was calculated according to European standards [40]. The value of the dilation angle was taken equal to 40° as suggested by Tao et al. [41] for infilled concrete. The default values of the viscosity parameter and flow potential eccentricity were taken as 0 and 0.1 respectively, as they have no significant influence on concrete-filled tubes [41]. The ratio of the compressive strength under biaxial loading to uniaxial compressive strength and the compressive meridian were determined according to [42]. When a CFAT member is axially compressed, the concrete infill expands laterally and interacts with the aluminium tube. To account for the composite action between the concrete infill and the aluminium tube, an equivalent uniaxial compressive stress-strain model of confined concrete [41-44] was considered. In this model, the ascending part of the stress-strain response of the confined concrete is taken similar to that of the unconfined concrete, considering no interaction. After the peak strength, the lateral strain of concrete increases and the concrete interacts with the hollow tube. Consequently, confining pressure develops between the two materials, improving the compressive strength of concrete. The beneficial effect of confinement in concrete's strength and ductility is simulated by considering the confined model shown in Figure 6. Based on the material test data, the compressive cylinder strength was taken equal to 25.25 MPa (80% of the cube strength). The tensile behaviour of concrete was assumed to be linear up to 10% of compressive cylinder strength [41]. The inelastic region of the concrete tensile stress-strain curve was defined according to the stress-crack opening displacement relationship [45], as a function of the fracture energy which was determined in line with [46, 47].

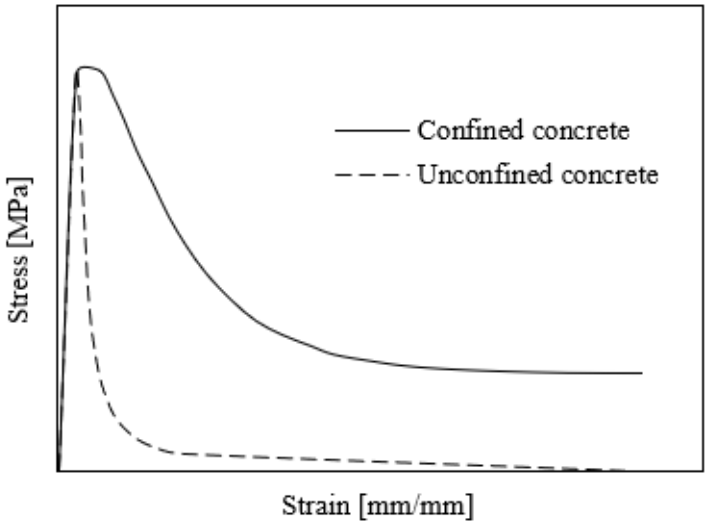

Figure 6. Stress-strain model for confined concrete proposed by Tao et al. [41].

The interaction between the aluminium tube and the concrete infill was simulated using the surface-to-surface contact. Thus, a contact pair was defined between the inner surfaces of the aluminium tube (slave surface) and the outer surfaces of the concrete infill (master surface). A hard contact pressure-overclosure relationship was assigned in the direction normal to the plane of these surfaces to simulate the development of normal stresses between surfaces without penetration in compression and releasing stresses by separating from each other in tension. The Coulomb friction model was adopted in the tangential direction for allowing slippage between the aluminium tube and concrete. As the compressive load was applied on both the aluminium tube and the concrete simultaneously, the possibility of slippage is almost negligible. Therefore, the results are less sensitive to the values of the friction coefficient. Based on the findings reported in [48], a value of 0.3 was used for the friction coefficient, which retains sufficient accuracy and offers a quick convergence.

To simulate the pin-ended boundary conditions, a reference point was created on the centroid of the cross-section for each column end by considering the effective height of specimens measured in the tests. Top and bottom reference points were fixed against all translational and rotational degrees of freedom except the longitudinal translation at the loaded end and the rotational about the examined buckling axis. In line with past studies [18, 50], the CFRP wraps were not explicitly modelled, but the prevention of a potential localised failure was considered through coupling constraints in the supports. Figure 7 shows the FE model of a typical CFAT column.

It is well documented that the compressive behaviour of a hollow column is significantly affected by the presence of initial geometric imperfections [22]. Towards this end, an eigenvalue buckling analysis was performed and the lowest local and global buckling modes were introduced as initial geometric imperfections in the nonlinear FE model. Figure 8 shows the typical mode shapes obtained from linear buckling analysis. The residual stresses caused by the heat-treatment of aluminium alloys are insignificant [49] and hence are neglected in this FE analysis [50, 51]. A nonlinear static analysis using the modified Riks solution method [38] was performed to capture the full nonlinear response of the columns. The axial compressive load was applied at the top reference point by specifying a displacement to replicate the loading condition used in the tests.

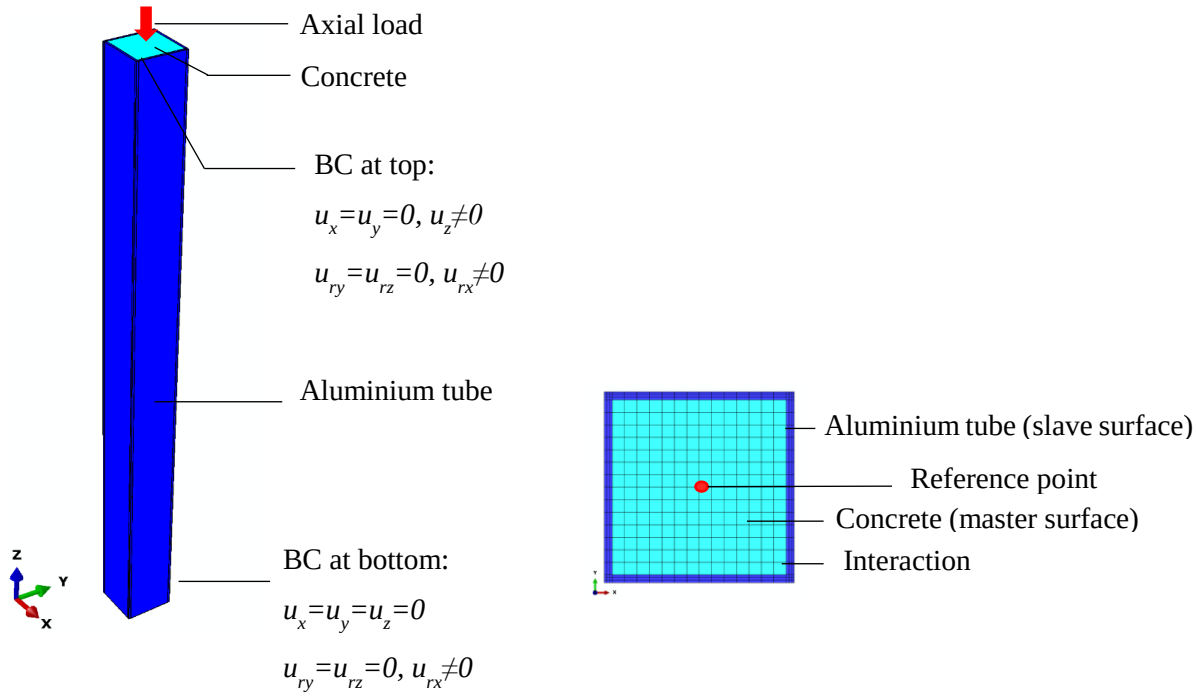

Figure 7: FE model of a typical CFAT column specimen.

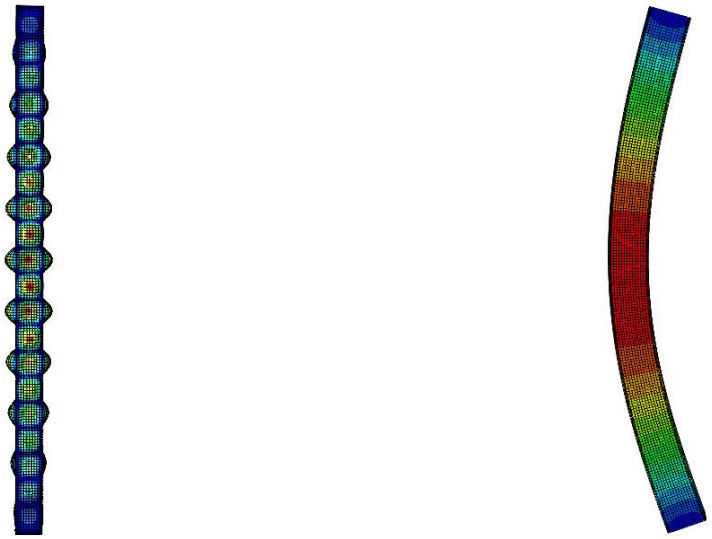

(a) Local (b) Global

Figure 8: Typical elastic buckling mode shapes.

3.2 Model validation

The eighteen specimens used in the experimental testing were used to validate the developed FE models based on the assumptions mentioned earlier. The accuracy of the models was evaluated by comparing the experimental and numerical results in terms of the ultimate capacities, load versus mid-height lateral displacement and failure modes.

An imperfection sensitivity study was conducted to determine suitable imperfection amplitudes to be considered in the subsequent parametric study. Four global imperfection amplitudes including the measured values and three fractions of the critical buckling length, i.e. L_{cr}/1000, L_{cr}/1500 and L_{cr}/2000 were considered. The measured global imperfection amplitudes were determined by summing the magnitudes of the initial bow and loading eccentricity. For the concrete-filled columns, the effect of initial local imperfections is negligible due to concrete infill and hence were not explicitly modelled [52, 53]. For the bare columns, in addition to global imperfection, local geometric imperfections with magnitude equal to 1/10 of the cross-sectional thickness were considered. This amplitude was based on the measured values (ω_l) and was found to provide accurate results. Table 5 presents the ratios of numerical to experimental values of ultimate capacities ($N_{u,FE}/N_{u,Exp}$) for a range of global imperfections. Overall, a fairly good agreement between the test and numerical data has been obtained with mean values close to unity. It can be seen that the global amplitude L_{cr}/1000 provided the most accurate predictions of ultimate capacities with mean value of $N_{u,FE}/N_{u,Exp}$ equal to 0.99. The

comparison between experimental and numerical (for global imperfection amplitude L_{cr}/1000) load versus mid-height lateral displacement curves of typical specimens is depicted in Figure 9, showing a good comparison. Moreover, successfully replicated failure modes by the FE models are illustrated in Figure 10. Overall, it can be concluded that the developed FE models are capable of accurately predicting the structural response of CFAT and BAT columns.

Table 5: Comparison of test and FE results for varying imperfection amplitudes.

Specimen	$N_{u,FE}/N_{u,Exp}$ Global Imperfection Amplitude			
	Measured	L_{cr}/1000	L_{cr}/1500	L_{cr}/2000
50.8×50.8×1.6	1.02	0.95	0.98	1.00
50.8×50.8×1.6-C	0.87	0.83	0.85	0.87
50.8×50.8×3.3	0.94	0.96	1.00	1.02
50.8×50.8×3.3-C	1.02	1.02	1.05	1.06
50.8×50.8×4.8	0.90	0.95	0.98	0.99
50.8×50.8×4.8-C	0.87	0.90	0.92	0.94
76.2×76.2×3.3	0.94	0.95	0.97	0.98
76.2×76.2×3.3-C	1.19	1.08	1.12	1.43
76.2×76.2×4.8	1.00	0.99	1.02	1.03
76.2×76.2×4.8-C	1.07	1.04	1.07	1.09
76.2×76.2×6.4	1.01	0.97	0.98	1.01
76.2×76.2×6.4-C	1.20	1.06	1.14	1.47
76.2×38.1×3.3	1.04	1.04	1.05	1.06
76.2×38.1×3.3-C	1.12	1.00	1.03	1.11
76.2×50.8×3.3	0.91	1.10	1.13	1.16
76.2×50.8×3.3-C	1.02	0.93	0.94	0.97
101.6×50.8×3.3	1.04	1.01	1.02	1.02
101.6×50.8×3.3-C	1.25	1.05	1.12	1.14
Mean	1.02	0.99	1.02	1.08
COV	0.11	0.07	0.08	0.14

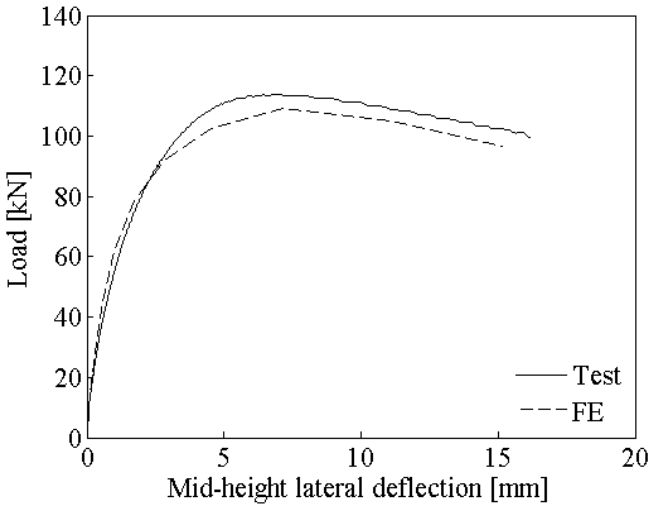

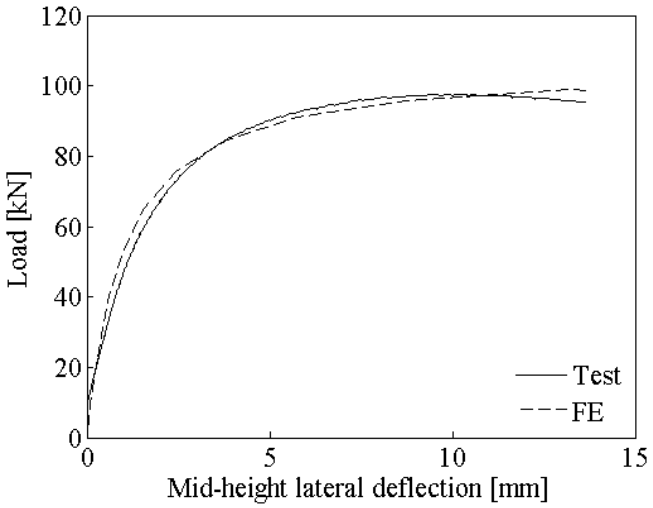

(a) 50.8×50.8×3.3

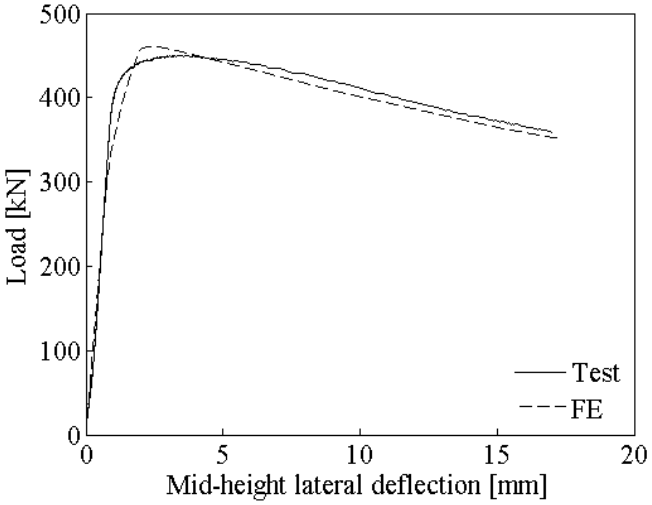

(b) 76.2×38.1×3.3

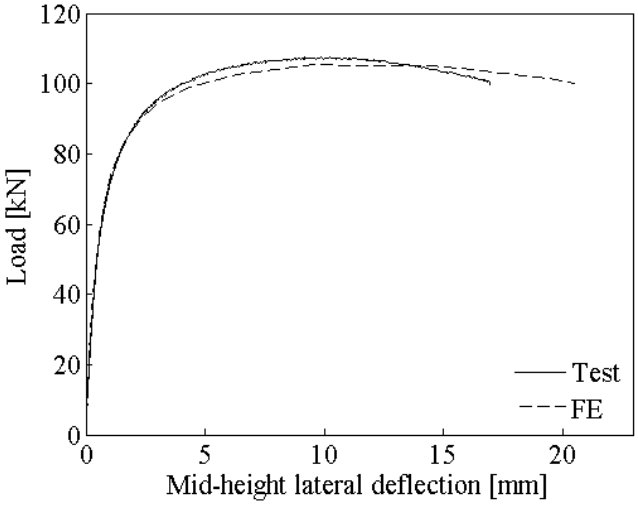

(c) 76.2×76.2×4.8-C

(d) 76.2×38.1×3.3-C

Figure 9: Experimental and numerical load–mid-height lateral deflection curves.

(a) 76.2×76.2×4.8-C

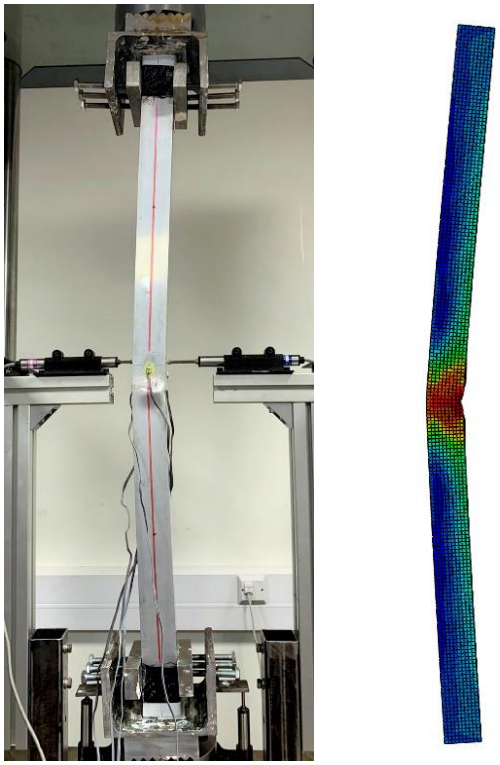

(b) 50.8×50.8×1.6

Figure 10: Experimental and numerical failure modes.

3.3 Parametric study

Based on the validated FE models, a parametric study was undertaken to generate additional structural performance data over a wide range of cross-sections and member slendernesses and to investigate the effect of the concrete infill. In total, 108 CFAT and BAT columns were modelled in this study. Square tubes with cross-sectional dimensions of 50×50 and wall thicknesses 1, 3 and 5 mm and rectangular tubes of 100×50 with 2, 6 and 10 mm thicknesses were considered. Both major and minor axis buckling was examined for rectangular BAT and CFAT columns. The specimen lengths were taken from 150 to 3000 mm and 500 to 2300 mm for BAT and CFAT columns, respectively, to cover a wide range of member slendernesses. Three different concrete cylinder strengths f'_c of 30, 50 and 70 MPa were considered for CFAT columns. Average measured stress-strain curves were defined for the aluminium alloy. The initial global imperfection amplitude of L_{cr}/1000 and the combination of initial local and global amplitudes of t/10 and L_{cr}/1000 were adopted for CFAT and BAT columns, respectively. These values were, also, employed successfully in similar studies [54,55].

Figure 11 presents typical load versus mid-height lateral deflection curves obtained from the FE parametric study. In particular, Figure 11(a) shows the response of a typical BAT column with constant cross-section and different member slenderness. In Figure 11(b), the FE buckling behaviour of CFAT columns with constant member length and different cross-sectional thickness is presented, showing higher load for lower cross-sectional slenderness. Figure 11(c) shows a comparison of a CFAT column with bucking about the major and minor axis, whilst in Figure 11(d), a comparison between CFAT and BAT columns is presented, demonstrating increased strength for concrete-filled members.

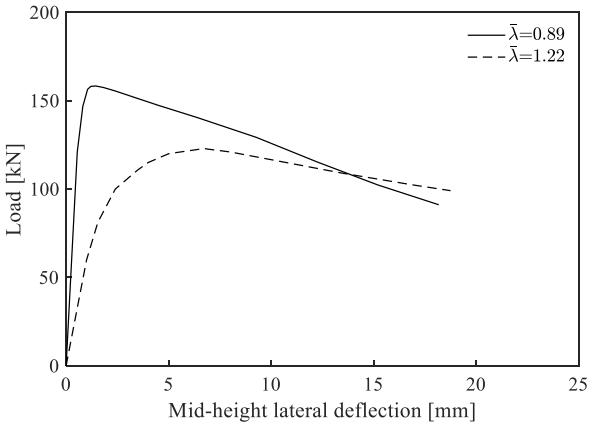

(a) BAT columns - 50×50×3

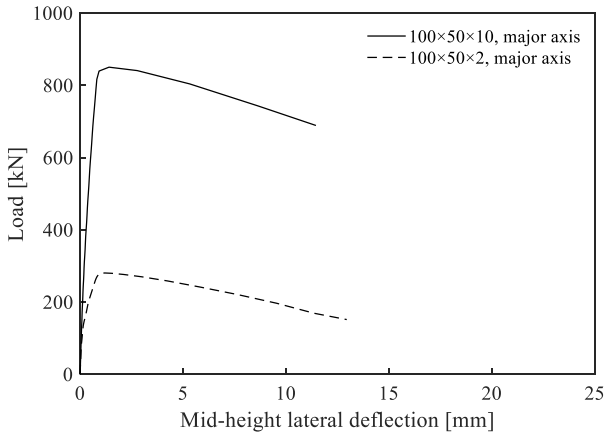

(b) CFAT columns - L_{cr}=1000 mm

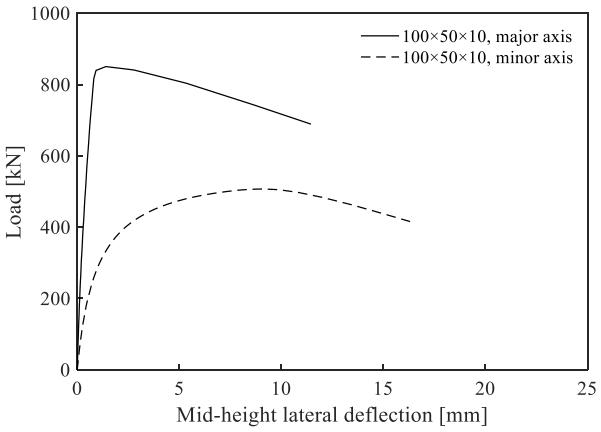

(c) CFAT columns - L_{cr}=1000 mm

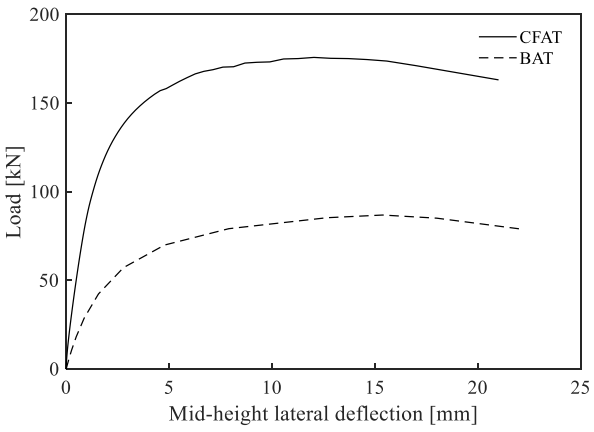

(d) CFAT and BAT column - 100×50×2, major axis, L_{cr}=2300 mm

Figure 11: Typical load-mid-height lateral deflection curves from FE studies.

Aiming to evaluate the effect of the concrete grade on the ultimate strength of CFAT columns, the ultimate FE load values were used. Figure 12 presents the percentage strength increase owing to higher concrete grade ($(N_{u,C50/70} - N_{u,C30})/N_{u,C30}$) with respect to the strength at C30 ($N_{u,C30}$) for typical CFAT columns of constant length. It can be seen that the strength increase owing to higher concrete grade seems to be more pronounced in columns with thinner plate elements (50×50×1 vs 50×50×5 and 100×50×2 vs 100×50×10). This has been observed for square tubes but also for the case of rectangular tubes under major and minor axis buckling. As will also be discussed in the following section, the buckling strength is a function of the cross-sectional plastic resistances of the two materials, concrete and aluminium. Hence for increased concrete strength, the concrete's cross-sectional plastic resistance increases as well. The latter comprises a bigger percentage of the total cross-sectional plastic resistance for slender sections (in which the aluminium cross-sectional area is small) which in turn leads to a more significant increase to the ultimate load for higher concrete grades.

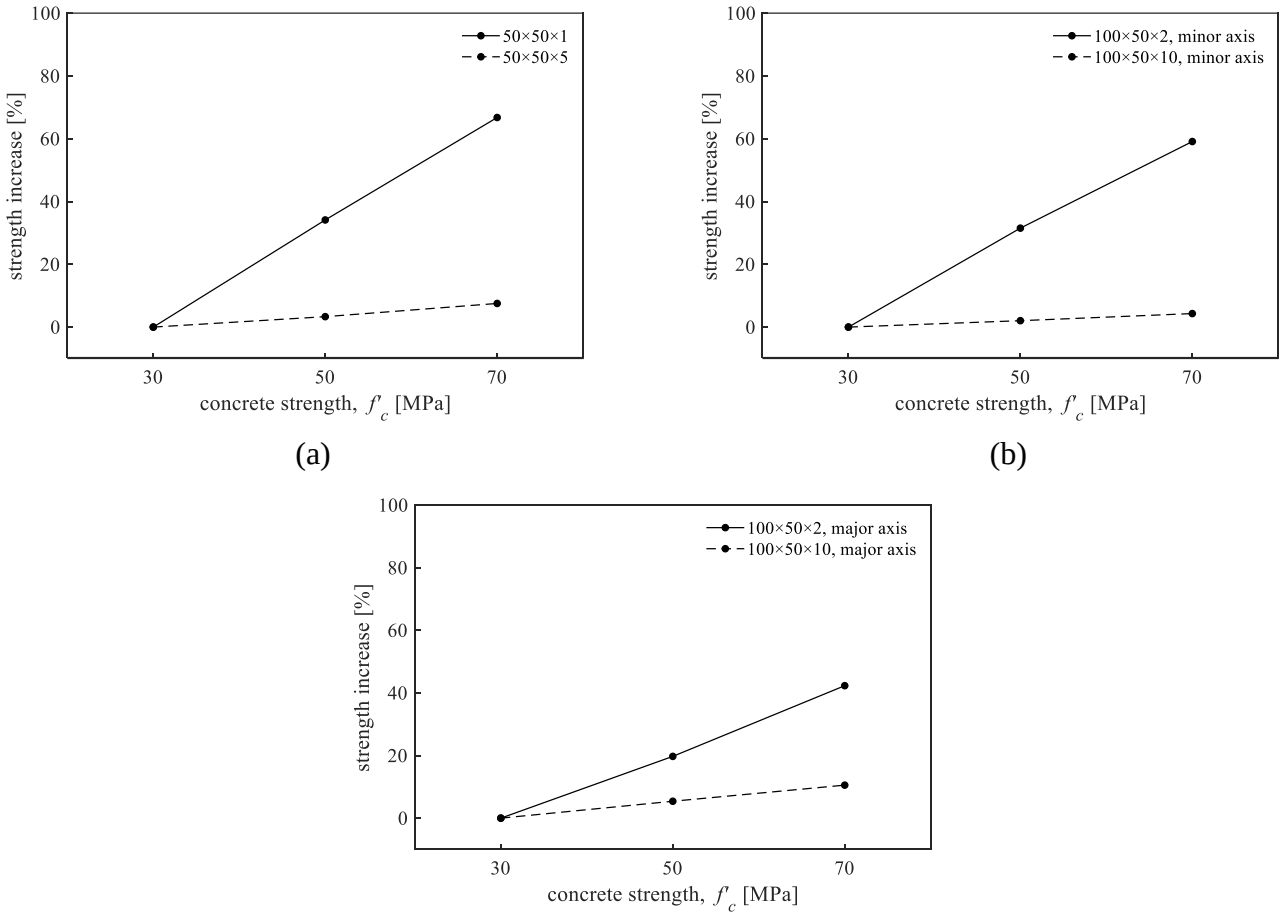

Figure 12: Effects of concrete compressive strengths, f'_c, on the ultimate strength of CFAT columns (L_{cr}=1000 mm).

4. Design recommendations

The experimental and numerical results are used to assess strength predictions of the current European standards and provide design recommendations for BAT and CFAT columns in Sections 4.1 and 4.2, respectively.

4.1 Strength prediction for BAT columns

For BAT columns, current Eurocode design equations are assessed and a proposal for improved strength predictions on the basis of experimental and numerical findings is made.

EN 1999-1-1 (EC9) [31] provides design rules for the strength of aluminium alloy columns under axial compression. The plastic cross-sectional resistance of square and rectangular bare columns is calculated by Eq. (4):

$$N_{pl,Rk} = A_a \sigma_{0.2} \tag{4}$$

where A_a the aluminium cross-sectional area for Classes 1-3 sections [31].

EN 1999-1-1 [31] adopts the cross-section classification for the treatment of local buckling in aluminium cross-sections under compression. The classification is based on the comparison of the β/ε ratio of the most slender constituent plate element with limit values defined in [31]. Moreover, EN 1999-1-1 [31] classifies the aluminium alloys in two material Classes, namely Class A and B, based on the temper designation. The herein examined 6082-T6 aluminium alloy is Class A and thus the relative coefficients in the following formulae correspond to Class A. In case of Class 4 sections, the A_a of Eq. (4) is substituted by the effective cross-sectional area ($A_{\alpha,eff}$), which is estimated by assuming a reduced thickness for the slender plate elements through a reduction factor, ρ_c :

$$\rho_c = \frac{32}{(\beta/\varepsilon)} - \frac{220}{(\beta/\varepsilon)^2} \tag{5}$$

The current EN 1999-1-1 [31] provisions for column strength adopt the buckling curve approach. The buckling resistance (N_{pred}) is found by Eq. (6)

$$N_{pred} = \chi N_{pl,Rk} \tag{6}$$

where the reduction coefficient χ is given by Eq. (7)

$$\chi = \frac{1}{\phi + \left[\phi^2 - \bar{\lambda}^2\right]^{0.5}} \leq 1.0 \tag{7}$$

The parameter ϕ and the member slenderness $\bar{\lambda}$ are calculated by Eqs. (8) and (9), respectively:

$$\phi = 0.5\left[1 + 0.2\left(\bar{\lambda} - 0.1\right) + \bar{\lambda}^2\right] \tag{8}$$

$$\bar{\lambda} = \sqrt{N_{pl,Rk} / N_{cr}} \tag{9}$$

Where 0.2 is the recommended value for the imperfection factor (α) for Class A aluminium alloys, 0.1 is the recommended limit of the horizontal plateau ($\bar{\lambda}_0$), and N_{cr} is the critical elastic buckling load, which is determined from Eq. (10):

$$N_{cr} = \pi^2 (E_a I_a) / L_{cr}^2 \quad (10)$$

where E_a is the Modulus of Elasticity of aluminium, I_a is the second moment of area of the aluminium tube and L_{cr} is the effective buckling column length.

In order to assess the accuracy of EN 1999-1-1 [31] strength predictions, Figure 13 depicts the ultimate loads (N_u) obtained from the experiments and the FE study normalised by the plastic resistance ($N_{pl,Rk}$) according to Eq. (4) and plotted against the member slenderness $\overline{\lambda}$. The Eurocode buckling design curve (EC9) is also included in this figure. It can be seen that both the experimental and FE data are above the design curve, which signifies that the design predictions by the EN 1999-1-1 [31] are conservative.

Table 6 lists the N_u / N_{EC9} ratios, where N_{EC9} is the N_{pred} found from Eq. (6) using EC9 buckling curve according to Eq. (8). The ratios are reported together with the corresponding member slendernesses, $\overline{\lambda}$, and the cross-sectional Class of the examined columns. Based on both the FE and test data, the mean value of N_u / N_{EC9} ratio is 1.20 indicating that EN 1999-1-1 [31] underestimates the actual buckling strength of bare columns. Moreover, the high value of COV reported in Table 6 and the scattered predictions graphically shown in Figure 13 suggest relatively low level of design consistency of the EN 1999-1-1 [31] strength predictions.

Aiming to improve the accuracy of the current design rules for BAT slender columns, a revised buckling curve is recommended. On the basis of the obtained test and FE results, Eq. (11) is proposed for the calculation of parameter ϕ for Class A aluminium alloys. This equation uses a revised imperfection factor (α), which is equal to 0.08, and a revised limit of the horizontal plateau ($\overline{\lambda}_0$), which is equal to 0.2:

$$\phi = 0.5\left[1 + 0.08\left(\overline{\lambda} - 0.2\right) + \overline{\lambda}^2\right] \quad (11)$$

The proposed buckling curve is shown in Figure 13, whilst the corresponding $N_u / N_{prop,BAT}$ ratios are included in Table 6. $N_{prop,BAT}$ is the N_{pred} found from Eq. (6), when applying Eqs. (4), (5), (7) and (9)-(11) (i.e. replacing current Eq. (8) with the proposed Eq. (11)). As can be seen, the proposed curve improves the accuracy of the predicted strength values by 12%. The same observations can be drawn from Figure 14, where the ultimate loads (N_u) are plotted

versus the strength predictions (N_{pred}), showing that the proposed curve provides better strength predictions (i.e. closer to diagonal line) compared to those of EC9.

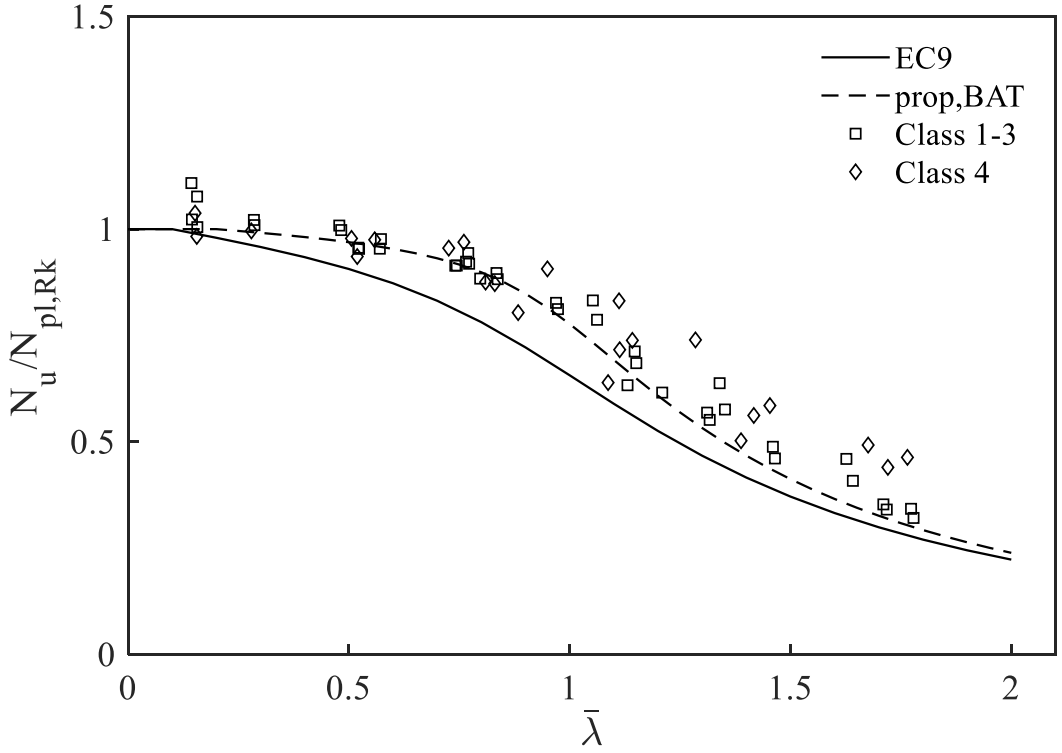

Figure 13: Comparison of experimental and numerical results with European and proposed design strengths for BAT columns.

Table 6: Predicted strength ratios for both experimental and numerical results for BAT columns.

Specimen	No	Class	$\bar{\lambda}$	$\frac{N_u}{N_{EC9}}$	$\frac{N_u}{N_{prop,BAT}}$
				Eqs. (4)-(10)	Eqs. (4)-(7) & Eqs. (9)-(11)
50.8×50.8×1.6	1	4	1.11	1.43	1.22
50.8×50.8×3.3	1	2	1.13	1.11	0.95
50.8×50.8×4.8	1	1	1.21	1.18	1.03
76.2×76.2×3.3	1	4	0.76	1.21	1.06
76.2×76.2×4.8	1	2	0.80	1.13	0.98
76.2×76.2×6.4	1	2	0.77	1.18	1.04
76.2×38.1×3.3	1	4	1.39	1.19	1.06
76.2×50.8×3.3	1	4	1.09	1.07	0.91
101.6×50.8×3.3	1	4	0.88	1.10	0.94
FE	36	1-3	0.14-1.78	1.13	1.06
	18	4	0.15-1.76	1.25	1.12
			mean (all)	1.20	1.08
			COV (all)	0.12	0.11

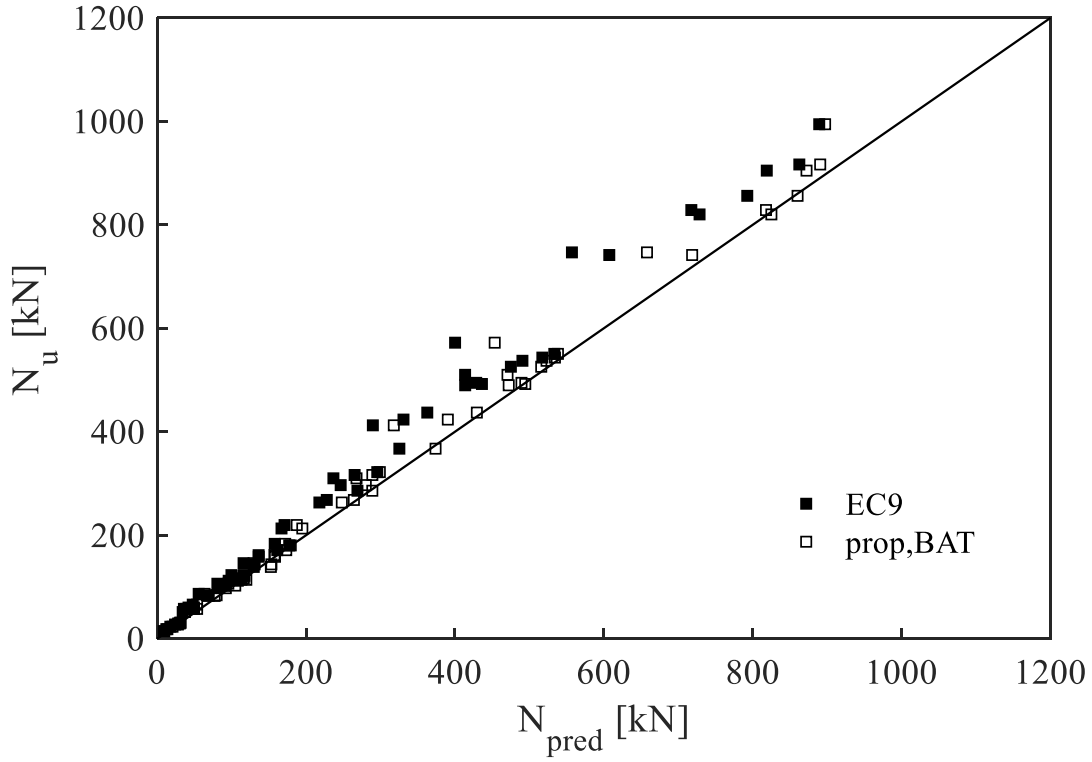

Figure 14: Comparison of experimental and numerical ultimate loads with design strengths based on European standards and proposed equations for BAT columns.

4.2 Strength prediction for CFAT columns

In absence of design provisions for the aluminium-concrete composite columns, the present study adopts the design methodology for composite steel-concrete members available in EN 1994-1-1 (EC4) [32] for the prediction of the ultimate capacities of CFAT columns, replacing appropriately the material properties of steel by those of the aluminium alloy and proposes a buckling curve for CFAT columns on the basis of the experimental and numerical data.

According to EN 1994-1-1 [32], the plastic cross-sectional resistance of square and rectangular concrete-filled columns can be calculated by Eq. (12):

$$N_{pl,Rk} = A_a \sigma_{0.2} + 0.85 A_c f_c^{'} \quad (12)$$

where A_c the cross-sectional area of concrete and f'_c the compressive cylinder strength of the concrete infill. The cross-section classification adopted by EN 1999-1-1 [31] is applied for the examined aluminium cross-sections. The member slenderness $\bar{\lambda}$ is calculated according to Eq. (9), where the critical elastic buckling load is taken as follows:

$$N_{cr} = \pi^2 (E_a I_a + k_e E_c I_c) / L_{cr}^{\ 2} \quad (13)$$

where E_c is the Modulus of Elasticity of concrete infill according to EN 1992-1-1 [40], I_c is the second moment of area of the concrete infill and k_e is the correction factor for the concrete which is taken equal to 0.6 [32].

Figure 15 shows the ultimate loads (N_u) obtained from the experiments and the FE study normalised by the plastic resistance ($N_{pl,Rk}$) from Eq. (12) and plotted against the member slenderness $\bar{\lambda}$ according to Eq. (9), separately for cross-section classes. In the same graph, a proposed buckling design curve is also displayed following the EC9 methodology but with the imperfection factor and limit of the horizontal plateau calibrated on the basis of the obtained data according to Eq. (14).

$$\phi = 0.5\left[1 + 0.18\left(\bar{\lambda} - 0.2\right) + \bar{\lambda}^2\right] \quad (14)$$

Based on Figure 15, it can also be observed that the Class 4 (slender) and Class 1-3 aluminium cross-sections follow a different trend, particularly for increasing member slenderness. This can also be considered together with the conclusion derived in Section 2.3, based on which the highest strength increase was noted for the most slender cross-section. In absence of sufficient

experimental data for concrete-filled slender aluminium square and rectangular hollow sections at cross-sectional level, the present proposal was based on the currently adopted equations of EC9 for local buckling (i.e. Eq. (5)). However, future studies on this direction are recommended to gain a better understanding of the cross-sectional resistance of CFAT cross-sections.

Implementing EC9 Eq. (5) for the effective cross-sectional area to account for local buckling in slender aluminium cross-sections, together with Eqs. (12)-(13) of EC4, Eqs. (7) and (9) of EC9 and the proposed Eq. (14) in place of Eq. (8), the proposed strength $N_{prop,CFAT}$ can be evaluated from Eq. (6). The ultimate over proposed strength values $N_u / N_{prop,CFAT}$ are summarised in Table 7. The resulting overall mean value is 1.13, whilst the strength is more accurately predicted for stocky aluminium cross-sections ($N_u / N_{prop,CFAT}$ equal to 1.05 for Class 1-3). These values indicate that the combined design formulae proposed herein provide good predictions with reasonable consistency. The same can, also, be concluded from Figure 16 where the examined N_{pred} values deviate slightly from the diagonal line with relatively low scattering.

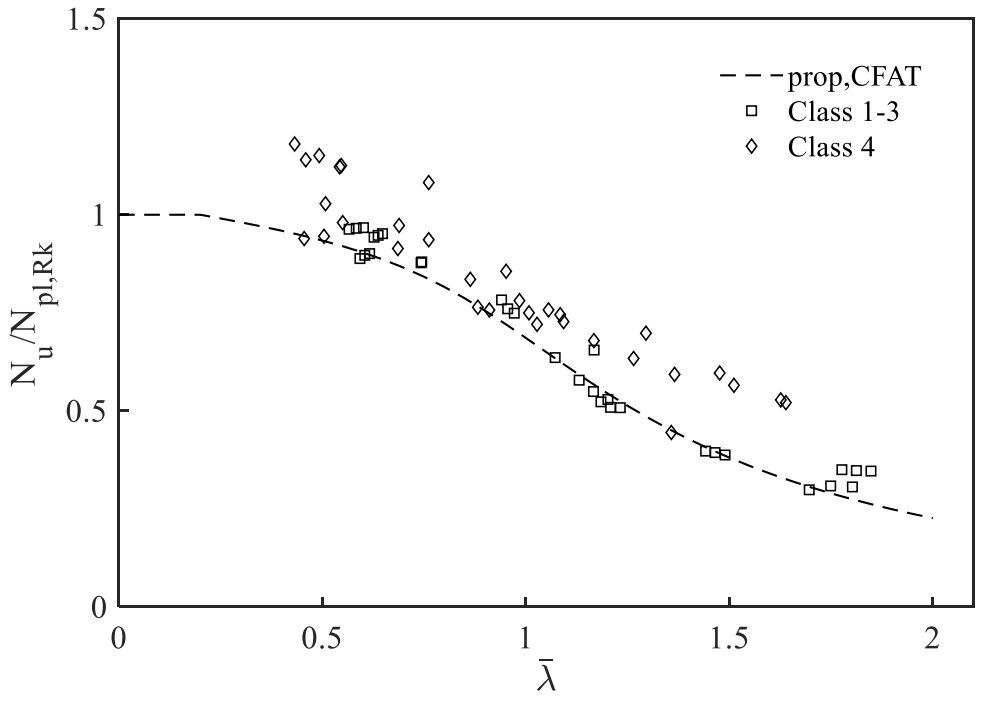

Figure 15: Comparison of experimental and numerical results with proposed design strengths for CFAT columns.

Table 7: Predicted strength ratios for both experimental and numerical results for CFAT columns.

Specimen	No	Class	$\overline{\lambda}$	$\frac{N_u}{N_{prop,CFAT}}$	
				Eqs. (5)-(7),(9) & Eqs. (12)-(14)	
				Class 1-3	Class 4
50.8×50.8×1.6-C	1	4	0.98	-	1.19
50.8×50.8×3.3-C	1	2	1.09	1.00	-
50.8×50.8×4.8-C	1	1	1.18	1.16	-
76.2×76.2×3.3-C	1	4	0.70	-	1.05
76.2×76.2×4.8-C	1	2	0.76	1.04	-
76.2×76.2×6.4-C	1	2	0.75	1.04	-
76.2×38.1×3.3-C	1	4	1.38	-	0.99
76.2×50.8×3.3-C	1	4	1.05	-	1.08
101.6×50.8×3.3-C	1	4	0.91	-	1.00
FE	31	1-3	0.57-1.85	1.08	-
	32	4	0.43-1.64	-	1.05
			Mean	1.05	1.20
			COV	0.09	0.14
			mean (all)	1.13	
			COV (all)	0.14	

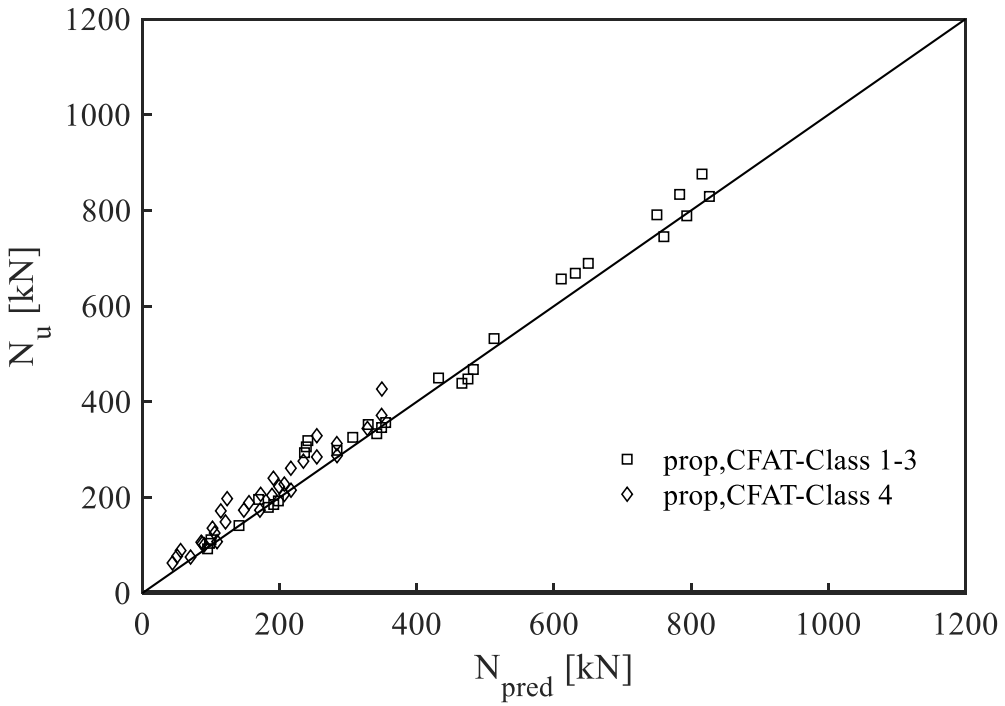

Figure 16: Comparison of experimental and numerical ultimate loads with proposed design strengths for CFAT columns.

5. Conclusions

A comprehensive experimental and numerical study was carried out to investigate the flexural buckling performance of BAT and CFAT columns, reaching the following conclusions:

(1) A total of 18 specimens, including 9 CFAT and 9 BAT 6082-T6 heat-treated aluminium alloy square and rectangular columns were tested. The predominant failure mode was flexural buckling.

(2) It was shown that the concrete infill effectively delays buckling. Consequently, the CFAT columns exhibited higher strength and stiffness compared to the BAT columns.

(3) Based on the experimental programme, the strength increase for constant member length owing to the concrete infill was more significant in case of slender cross-sections. The highest increase, which was equal to 72%, has been observed for the most slender cross-section and can be attributed to the delay in the local buckling offered by the concrete infill.

(4) It was demonstrated that the developed FE models with a global imperfection magnitude of L_{cr}/1000 could accurately capture the structural response of CFAT and BAT columns. Hence, a parametric study, including 108 columns was performed.

(5) Based on the FE study, the strength increase for constant member length owing to higher concrete grade appeared more pronounced for slender cross-sections. Future research to verify this conclusion in a wide variety of cross-sections and aluminium alloys is recommended.

(6) The comparison between the European provisions and the experimental and FE results for BAT slender columns showed that the current codified equations underestimate the actual strength of BAT slender columns.

(7) A revised buckling curve was proposed for BAT columns which was able to improve the strength prediction of square and rectangular Class A aluminium tubes by 12% compared to that of EC9.

(8) In absence of design provisions for aluminium-concrete composite columns, the present study proposed adopting the European design formulae for composite steel-concrete members with the material properties of steel replaced by those of aluminium alloy. A new buckling design curve was proposed on the basis of the experimental and numerical data and used in conjunction with the European standards. The proposal was found to be suitable for the design of CFAT columns providing reasonably accurate and consistent strength predictions.

(9) A different trend has been observed on the performance of CFAT columns comprising Class 4 aluminium sections. Further research is recommended to evaluate the cross-sectional performance of concrete-filled Class 4 aluminium square and rectangular tubes.

Acknowledgements

The authors are grateful to the technicians of the School of Civil Engineering and Built Environment and School of Engineering at Liverpool John Moores University for their valuable assistance. Also, the financial support of the Faculty of Engineering and Technology of Liverpool John Moores University is gratefully acknowledged.

References

[1] Mazzolani FM. Competing issues for aluminium alloys in structural engineering. Prog Struct Eng Mater. 2004; 6(4):185–96.

[2] Shanmugam NE, Lakshmi B. State of the art report on steel–concrete composite columns. J Constr Steel Res. 2001; 10:1041–80.

[3] Lam D, Wong, K. Axial capacity of concrete filled stainless steel columns. ASCE Journal of Structures. 2005; 1107–20.

[4] Starossek U, Falah N, Lohning T. Numerical analyses of the force transfer in concrete-filled steel tube columns. Structural Engineering and Mechanics. 2010; 35(2):241–56.

[5] Vipulkumar IP, Uy B, Prajwal KA, Aslani F. Confined concrete model of circular, elliptical and octagonal CFST short columns. Steel Compos. Struct. 2016; 3:497–520.

[6] Liu S, Xinxin D, Li X, Liu Y, Zhao S. Behavior of rectangular-sectional steel tubular columns filled with high-strength steel fiber reinforced concrete under axial compression. Materials 2019; 12(17):2716.

[7] Ren Q, Li M, Zhang M, Shen Y, Si W. Prediction of ultimate axial capacity of square concrete-filled steel tubular short columns using a hybrid intelligent algorithm. Appl. Sci. 2019; 9:2802.

[8] Patel V, Liang Q, Hadi M. Numerical simulations of circular high strength concrete-

filled aluminum tubular short columns incorporating new concrete confinement model. Thin-Walled Struct. 2020; 147:106492.

[9] He L, Lin S, Jiang H. Confinement effect of concrete-filled steel tube columns with infill concrete of different strength grades. Frontiers in Materials. 2019; 6:71.

[10] Dong CX, Kwan AKH, Ho JCM. A constitutive model for predicting the lateral strain of confined concrete. Eng Struct. 2015; 91:155–66.

[11] Kinoshita M, Kotsovos MD, and Pavlovic MN. Behavior of concrete under passive confinement. J. Mater. Conc. Struct. Pavements. 1994; 502:131–42.

[12] Han LH, Zhao XL, Tao Z. Concrete-filled thin-walled steel SHS and RHS beam-columns subjected to cyclic loading. Thin-Walled Struct. 2003; 41(9):801–833.

[13] Fam A, Qie FS, Rizkalla S. Concrete filled steel tubes subjected to axial compression and lateral cyclic loads. J Struct Eng. 2004; 130(4):631–640.

[14] Yu Q, Tao Z, Wu Y. Experimental behaviour of high performance concrete filled steel tubular columns. Thin-Walled Struct. 2008; 46(4):362–370.

[15] Khaloo A, Raisi EM, Hosseini P, Tahsin H. Mechanical performance of self-compacting concrete reinforced with steel fibers. Constr Build Mater. 2004; 51(1):179–186.

[16] Zhou F, Young B. Tests of concrete-filled aluminum stub columns. Thin-Walled Struct. 2008; 46(6):573–83.

[17] Zhou F, Young B. Concrete-filled aluminum circular hollow section column tests. Thin-Walled Struct. 2009; 47(11):1272–1280.

[18] Zhou F, Young B. Numerical analysis and design of concrete-filled aluminum circular hollow section columns. Thin-Walled Struct. 2012; 50:45–55.

[19] Wang F, Zhao H, Han L. Analytical behavior of concrete-filled aluminum tubular stub columns under axial compression. Thin-Walled Struct. 2019; 140:21–30.

[20] Feng R, Chen Y, Gong W. Flexural behaviour of concrete-filled aluminium alloy thin-walled SHS and RHS tubes. Eng Struct. 2017; 137:33–49.

[21] Chen Y, Feng R, Gong W. Flexural behavior of concrete-filled aluminum alloy circular

hollow section tubes. Constr Build Mater. 2018; 165:295–319.

[22] Chen Y, Feng R, Xu J. Flexural behaviour of CFRP strengthened concrete-filled aluminium alloy CHS tubes. Constr Build Mater. 2017; 142:295–319.

[23] Zhu Y, Chen Y, Heb K, Feng R, Zhang X, Zhu Q, Tang C. Flexural behavior of concrete-filled SHS and RHS aluminum alloy tubes strengthened with CFRP. Compos Struct. 2020; 238:111975.

[24] Zhou F, Young B. Concrete- filled double-skin aluminum circular hollow section stub columns. Thin-Walled Struct. 2018; 133:141–52.

[25] Zhou F, Young B. Compressive strengths of concrete-filled double-skin (circular hollow section outer and square hollow section inner) aluminium tubular sections. Adv Struct Eng. 2019; 1–17.

[26] Patel V, Liang Q, Hadi M. Numerical study of circular double-skin concrete-filled aluminum tubular stub columns. Eng Struct. 2019; 197:109418.

[27] Guler S, Yavuz D, Aydına M. Hybrid fiber reinforced concrete-filled square stub columns under axial compression. Eng Struct. 2019; 198:109504.

[28] Georgantzia E, Gkantou M, Kamaris GS Aluminium alloys as structural material: A review of research. Eng Struct. 2020; 227:111372.

[29] Kissell J, Ferry R. Aluminum structures: a guide to their specifications and design. New York John Wiley Sons. 2002;

[30] Mazzolani F. Aluminium alloy structures. 2nd ed London Chapman Hall. 1995;

[31] European Committee for Standarization (EC9), Eurocode 9 : Design of aluminium structures. Part 1-1: General structural rules - General structural rules and rules for buildings. BS EN 1999-1-1:2007, CEN: 2007, BSI, 2007.

[32] European Committee for Standardisation (EC4), Eurocode 4: Design of Composite Steel and Concrete Structures. Part 1-1: General Rules and Rules for Buildings. BS EN 1994-1-1: 2004, CEN: 2004, BSI, 2004.

[33] Sun Y, He A, Liang Y, Zhao O. Flexural buckling behaviour of high-chromium stainless steel welded I-section columns. Thin-Walled Struct. 2020; 154:106812.

[34] EN ISO 6892-1, Metallic Materials – Tensile Testing – Part 1: Method of test at room temperature. European Committee for Standardization (CEN), Brussels, 2009.

[35] Ramberg W, Osgood WR. (1943). Description of stress-strain curves by three parameters. Technical Note No. 902. Washington, D.C., USA: National Advisory Committee for Aeronautics, 1943.

[36] Hill HN. (1944). Determination of stress-strain relations from "offset" yield strength values, Technical Note No. 927; 1944.

[37] Zhao O, Gardner L, Young B. Testing and numerical modelling of austenitic stainless steel CHS beam–columns. Eng Struct. 2016; 111:263-274.

[38] Karlsson Hibbitt, Sorensen, Inc. ABAQUS. ABAQUS/Standard User's Manual Volumes I-III and ABAQUS CAE Manual, 2016. Pawtucket (USA), Version 2016.

[39] Milan CC, Albareda-Valls A, Carreras J. Evaluation of structural performance between active and passive preloading systems in circular concrete-filled steel tubes (CFST). Eng Struct. 2019; 194:207–219.

[40] European Committee for Standardisation (EC2). Eurocode 2: Design of Concrete Structures. Part 1-1: General rules and rules for buildings. BS EN 1992-1-1: CEN: 2004. BSI; 2004.

[41] Tao Z, Wang ZB, Yu Q. Finite element modelling of concrete-filled steel stub columns under axial compression. J Constr Steel Res. 2013; 89:121–131.

[42] Yu T, Teng J, Wong Y, Dong S. Finite element modeling of confined concrete-I: Drucker-Prager type plasticity model. Eng Struct. 2010;32(3):665–679.

[43] De Nicolo B, Pani L, Pozzo E. Strain of concrete at peak compressive stress for a wide range of compressive strengths. Mater Struct. 1994;27(4):206–210.

[44] Samani A, Attard M. A stress–strain model for uniaxial and confined concrete under compression. Eng Struct. 2012; 41:335–349.

[45] Hordijk D. Local approach to fatigue of concrete. Ph D thesis Delft Univ Technol Delft, Netherlands. 1991.

[46] FIP. Ceb-Fip Model Code 1990. Ceb-Fip Model Code 1990. 1993.

[47] Bažant Z, Becq-Giraudon E. Statistical prediction of fracture parameters of concrete and implications for choice of testing standard. Cem Concr Res. 2002; 32(4):529–556.

[48] Dai X, Lam D. Numerical modelling of the axial compressive behavior of short concrete-filled elliptical steel columns. J Constr Steel Res. 2010; 66(7):931–942.

[49] Mazzolani FM, Residual Stress Tests Alu-Alloy Austrian Profiles, ECCS Committee, Brussels, 1975 Technical Report, Doc 16-75-1.

[50] Feng R, Liu J. Numerical investigation and design of perforated aluminium alloy SHS and RHS columns. Eng Struct. 2019; 199:109591.

[51] Wang F, Young B, Gardner L. Compressive testing and numerical modelling of concrete-filled double skin CHS with austenitic stainless steel outer tubes. Thin-Walled Struct. 2019;141: 345–359.

[52] Gardner L, Talja A, Baddoo N. Structural design of high-strength austenitic stainless steel. Thin-Walled Struct. 2006; 44(5):517–528.

[53] Tao Z, Uy B, Liao FY, Han LH. Nonlinear analysis of concrete-filled square stainless steel stub columns under axial compression. J Constr Steel Res. 2011; 67:1719–1732.

[54] Zhao Y, Zhai X, Sun L. Test and design method for the buckling behaviors of 6082-T6 aluminum alloy columns with box-type and L-type sections under eccentric compression. Thin-Walled Struct. 2016; 100:62-80.

[55] Chang Y, Liu M, Wang P. Interacted buckling failure of thin-walled irregular-shaped aluminum alloy column under axial compression. Thin-Walled Struct. 2016; 107:627-647.